



Sliding ferroelectricity in bilayer honeycomb structures: A first-principles studyZhe Wang ¹, Zhigang Gui,^{1,2,*} and Li Huang ^{1,†}¹*Department of Physics & Academy for Advanced Interdisciplinary Studies,
Southern University of Science and Technology, Shenzhen 518055, China*²*Guangdong Provincial Key Laboratory of Computational Science and Material Design,
Southern University of Science and Technology, Shenzhen, Guangdong 518055, China*

(Received 11 October 2022; revised 11 December 2022; accepted 13 January 2023; published 24 January 2023)

The sliding ferroelectricity is engineered by artificially stacking the nonpolar two-dimensional (2D) materials, which greatly broadens the 2D ferroelectrics from very few candidate materials to a large family of 2D materials. However, the electric polarizations are generally small due to the weak van der Waals interlayer interaction. The search for 2D sliding ferroelectrics with large polarization presents an ongoing challenge. Here we systematically investigate the sliding ferroelectricity in the bilayer honeycomb structures of BX ($X = \text{P, As, Sb}$), YN ($Y = \text{Al, Ga, In}$), and ZC ($Z = \text{Si, Ge, Sn}$) based on first-principles calculations. It is shown that the electric polarization decreases with the increase of the interlayer distance, and increases with the difference in electronegativity of the two constituent elements. Such dependence is further corroborated by a simple model. It is interesting to see that GeC can be an ideal sliding ferroelectric material with high polarization and energetically favorable polar stacking. Our results reveal the key factors in determining the electric polarization, which could facilitate the search and design of 2D sliding ferroelectrics with large out-of-plane polarization.

DOI: [10.1103/PhysRevB.107.035426](https://doi.org/10.1103/PhysRevB.107.035426)**I. INTRODUCTION**

Two-dimensional (2D) materials have attracted great attention since the discovery of graphene due to their remarkable advantages, which not only provide a new platform to study an abundance of physical phenomena, such as spintronics and valleytronics [1–3], but also open up unprecedented opportunities in nanoelectronics and optoelectronics [4–6]. Among them, 2D ferroelectric materials are an important class of functional materials with reversible spontaneous electric polarization, especially those with out-of-plane electric polarization, which is more favorable since most technologies are related to the electric polarizability perpendicular to the plane [7–10]. Researchers have found some exotic phenomena in 2D ferroelectrics, such as giant negative electrostriction [11], high tunneling electroresistance [12], and negative capacitance [13]. However, so far, the out-of-plane ferroelectricity was confirmed experimentally in only CuInP_2S_6 [14–16], $\alpha\text{-In}_2\text{Se}_3$ [17–19], and $\text{d}1\text{T-MoTe}_2$ [20] down to the monolayer limit. Their Curie temperatures (T_C) are above room temperature, and their magnitudes of electric polarization are mainly in the order of 10^{-11} C/m. The structural origin of ferroelectricity in these 2D materials results from the symmetry breaking of space inversion, which is similar to that of traditional perovskite ferroelectric materials [21]. For instance, the ferroelectric structure of $\alpha\text{-In}_2\text{Se}_3$ originates from the displacement of the central layer selenium atoms [22]. Despite

many 2D materials reported in the literature, the out-of-plane 2D ferroelectrics are still quite rare.

Sliding ferroelectricity was theoretically proposed by Wu *et al.* in 2017 [23]. It opens an attractive avenue to construct out-of-plane ferroelectricity in 2D materials out of centrosymmetric 2D nonpolar materials, of which the out-of-plane electric polarization arises from the ingenious assembly of their nonpolar monolayers through weak van der Waals interactions [24,25]. More interestingly, the reversal of the out-of-plane electric polarization can be induced by translational sliding of one monolayer with respect to the other without any requisite atomic displacements in the out-of-plane direction, which is distinctly different from the behaviors of traditional ferroelectrics. The sliding ferroelectricity has been extensively studied by first-principles calculations, such as BN [23,26,27], WTe_2 [28,29], MoS_2 [23,30], VS_2 [31], ZrI_2 [32–34], FeCl_2 [35], MoSi_2N_4 [36], Bi_2Te_3 [37], and phosphorene [38]. Among them, such intriguing ferroelectricity of BN [39,40], MX_2 ($M = \text{Mo and W, } X = \text{S and Se}$) [41], WTe_2 [42], and ReS_2 [43] has been experimentally confirmed recently. Besides the possible merits of conventional 2D ferroelectrics, sliding ferroelectrics usually shows temperature-independent properties such as the polarization can sustain a wide range of temperatures including room temperature [39].

However, the magnitudes of the electric polarizations in these sliding ferroelectric systems are generally small [25], with most of them being in the order of 10^{-12} C/m. Generally, the polarization can be well estimated by $p = Z_{\text{eff}}D$ in conventional ferroelectrics, where the electric dipole moment per unit cell (p) is roughly proportional to the off-center distortion (D) and Born effective charge (Z_{eff}), while in a

*guizg@sustech.edu.cn

†huangl@sustech.edu.cn

sliding ferroelectric material, such a simple relation cannot hold since the polarization does not stem from ionic displacements. Therefore, questions remain to be answered such as what the influential factors to the electric polarization are and how to enlarge them in 2D sliding ferroelectric materials. In addition, the experimental method for fabricating sliding ferroelectricity is comparatively complicated because the polar stacking configuration is usually not the most energetically favorable. Is there any 2D sliding ferroelectric of which the polar stacking can be energetically more stable in the ferroelectric phase than other stackings in nonpolar phases?

To resolve these issues, first-principles calculations are performed to systematically investigate the sliding ferroelectricity in the bilayer honeycomb structures, including BX ($X = \text{P, As, Sb}$), YN ($Y = \text{Al, Ga, In}$), and ZC ($Z = \text{Si, Ge, Sn}$). Our calculations not only identify a few promising sliding ferroelectrics with large out-of-plane electric polarization, but also demonstrate that the magnitude of electric polarization with complicated dependence on the anion type as in BX ($X = \text{P, As, Sb}$) or the cation type in YN ($Y = \text{Al, Ga, In}$) and ZC ($Z = \text{Si, Ge, Sn}$). The effect of the interlayer distance on the electric polarization is also discussed. Specifically, the electric polarization is shown to decrease (increase) with the increase of the interlayer distance (the difference in electronegativity of the two constituent elements). Furthermore, a simple model based on the point charge picture has been proposed to help us understand these relationships. For the stability of various stackings, our calculations reveal that the polar stacking configuration is not the most energetically favorable in most of the systems studied here, except for GeC.

II. COMPUTATIONAL DETAILS

The first-principles calculations are performed using the Vienna Ab Initio Simulation Package (VASP) [44], based on density functional theory (DFT) within the projector-augmented wave (PAW) method [45,46]. The exchange and correlation functional is treated using the Perdew-Burke-Ernzerhof (PBE) parametrization of the generalized gradient approximation (GGA) [47]. The energy cutoff of the plane wave basis is set to 500 eV. Electronic minimization is performed with an energy tolerance of 10^{-5} eV, and ionic relaxation is performed with a force tolerance of 0.01 eV/Å on each ion. The 2D systems are modeled with slabs containing a vacuum region of thickness more than 15 Å. A Γ -centered $20 \times 20 \times 1$ Monkhorst-Pack [48] k mesh is used for Brillion zone sampling. The climbing image nudged elastic band method is used to determine the energy barriers of various kinetic processes [49]. In addition, the van der Waals corrections are included as parametrized in the semiempirical DFT-D3 method [50]. To check dynamic stability, the phonon frequency is calculated with a $3 \times 3 \times 1$ supercell using the PHONOPY code [51].

III. RESULTS AND DISCUSSION

A. Identification of the polar stacking configuration in bilayer structures

The monolayer of group III-V and group IV binary compounds studied in this work have the same crystal structure

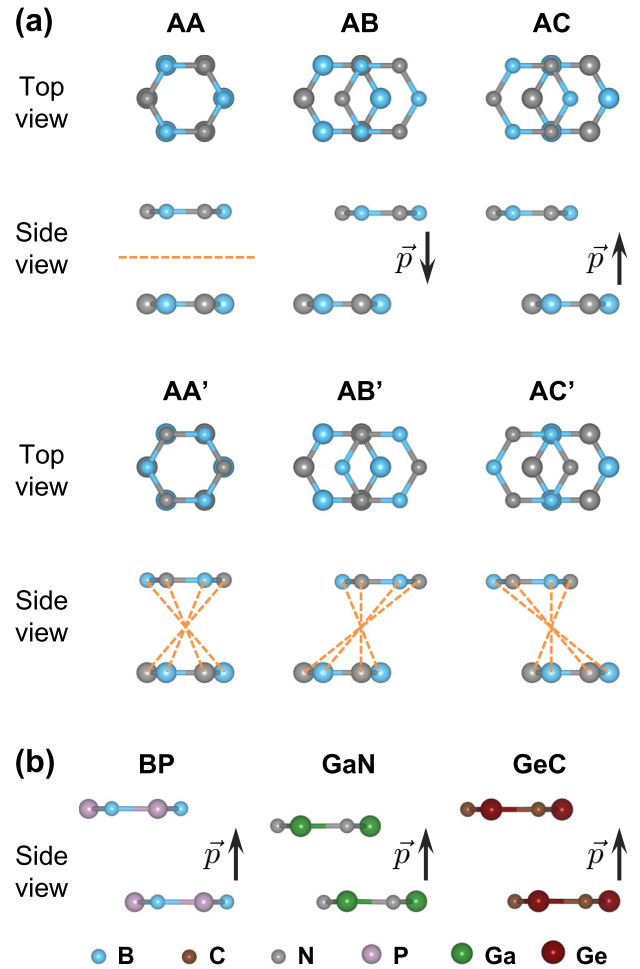


FIG. 1. Schematic diagram of atomic structures of the stacked bilayer. (a) Top and side views of six general high-symmetry stacking configurations, where the orange dashed line indicates the mirror or inversion symmetry for those non-polar stacking configurations. (b) Side views of BP, GaN, and GeC in the AC stacking configuration. The black arrows indicate the directions of the out-of-plane electric polarization.

as BN, a one-atomic-layered 2D crystal comprised of alternating B and N atoms in a honeycomb lattice. Their stable structures are planar, which is consistent with the previous work [52]. Here we focus on the bilayer structure, whose unit cell contains four atoms. The two chemically inequivalent atoms within one layer are bound by strong sp^2 covalent bonds, whereas the adjacent layers are coupled by weak van der Waals forces, which allows various stacking configurations between them. Using BN as an example, the six high-symmetry stacking configurations are shown in Fig. 1(a), wherein they are denoted as AA (eclipsed with N over N and B over B), AB (staggered with B over N), AC (staggered with N over B), AA' (eclipsed with B over N and N over B), AB' (staggered with N over N), and AC' (staggered with B over B), respectively. It is readily seen that the different stacking configurations can be transformed into each other by translational sliding, or by rotation of the basal plane around the vertical axis and a subsequent lateral sliding of one layer with respect to the other. Starting with the AA and AA'

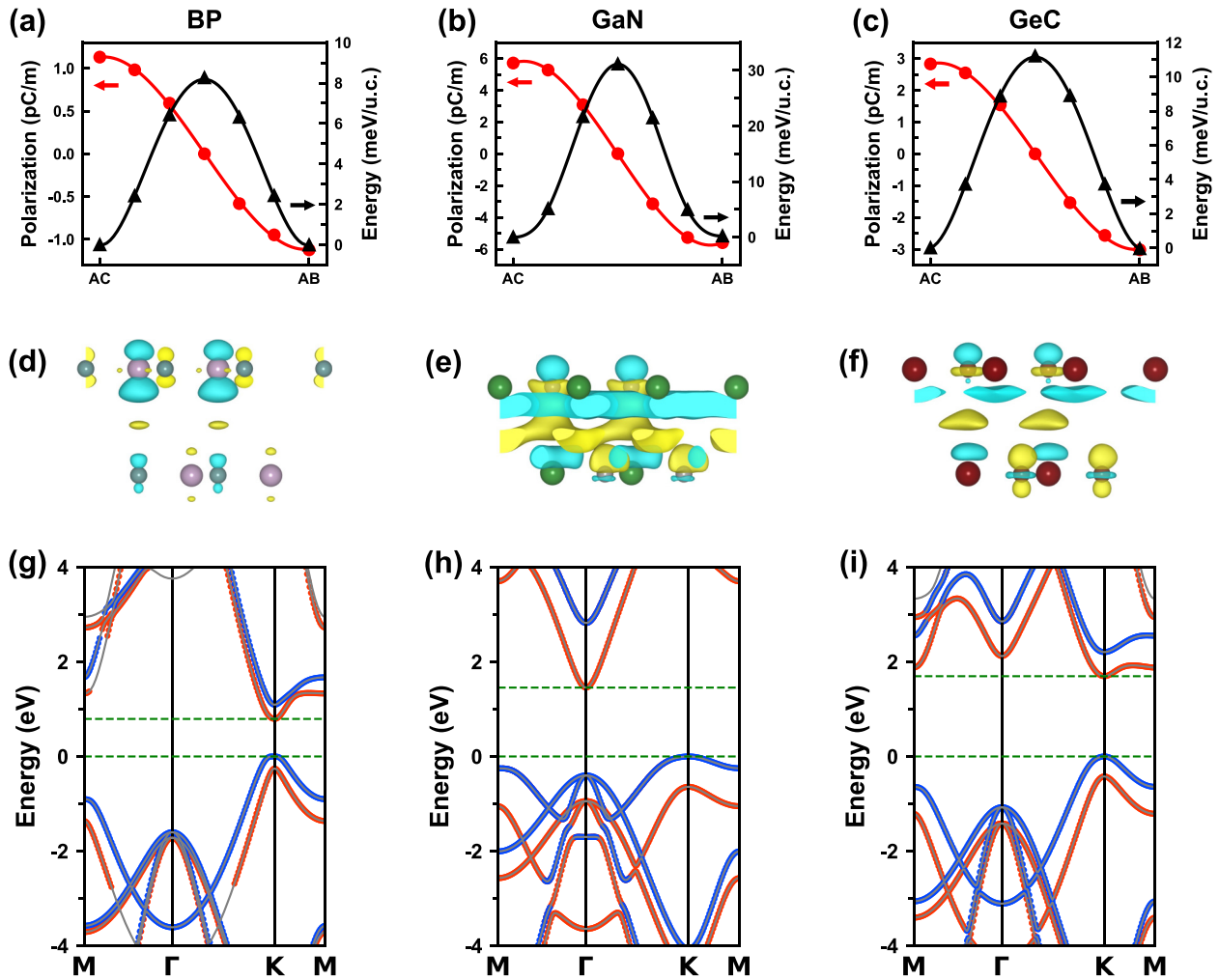


FIG. 2. Sliding ferroelectricity of BP, GaN, and GeC. (a)–(c) Reversal out-of-plane electric polarization (red curve with dots) and corresponding energy barrier (black curve with triangles) between AC and AB stacking configurations. (d)–(f) Differential charge density with an isosurface value of $0.00025 e/\text{\AA}^3$, where the yellow and cyan areas represent electron accumulation and depletion, respectively. (g)–(i) Layer-projected band structures, where the energy bands derived from upper and lower layer are highlighted in red and blue, respectively. The Fermi level of each system is shifted to energy zero in all the band structures.

stacking, a thorough search is performed for possible stacking configurations along the high-symmetry path (see Fig. S1 in the Supplemental Material [53]). The polarizations for several representative systems are shown in Fig. S1(b) as a function of the lateral shift. One can see that the out-of-plane electric polarization is only present in AB and AC stacking, which have degenerate energy but opposite polarization directions. Several representative systems in the AC stacking configuration are shown in Fig. 1(b), where the differences are mainly in the interlayer distances and in-plane lattice constants.

B. System-dependent sliding ferroelectricity

In the following section, we will discuss in detail the magnitudes of the out-of-plane electric polarizations in the AC stacking configuration of bilayer BX ($X = \text{P, As, Sb}$), YN ($Y = \text{Al, Ga, In}$), and ZC ($Z = \text{Si, Ge, Sn}$), respectively, as well as their energy barriers of polarization reversal and electronic properties.

BP, BAs, and BSb have the same cation as BN. The calculated magnitudes of polarizations for BP, BAs, and BSb are 1.075, 0.965, and 3.707 pC/m, respectively. Compared with BN (0.879 pC/m), the replacement of anion (N replaced by P or As) only slightly increases the polarization, except for BSb, whose large electric polarization comes from the combination of two kinds of polarization, one induced by interlayer interactions and the other by the spontaneous buckled monolayer in the stacked bilayer, as shown in Fig. S2 in the Supplemental Material [53]. The polarization direction can be reversed by the relative translational sliding between the two layers (transition between the AC and AB stacking configurations), and the corresponding energy barrier is 8 meV per unit cell for BP [see Fig. 2(a)], which is slightly higher than that of BN (3 meV per unit cell). The barriers are 12 and 195 meV per unit cell for BAs and BSb, respectively. The significant increased barrier of BSb is related to the stronger interlayer interactions due to the relatively small interlayer distance and the tendency to form covalent bonds between the layers [54]. Given the experimental evidence of the reversal

TABLE I. Summary of the calculated results for the considered systems. Lattice constant (a), electric polarization (P), ratio of electronegativity (E_a/E_c), effective distance $d_{\text{eff}} = d - d_{\text{bond}}$, where d and d_{bond} indicate the interlayer distance and the length of covalent bond between two constituent elements within monolayer, respectively, energy difference (ΔE) of the AA' (AC' for BP, BAs, and BSb) with respect to the AC, energy barrier of the polarization reversal between two polarized states, geometry of the monolayer in the polar stacking configurations are given.

System	a (Å)	P (pC/m)	E_a/E_c	d (Å)	d_{bond} (Å)	d_{eff} (Å)	ΔE (meV/u.c.)	Barrier (meV/u.c.)	Geometry
BN	2.513	0.879	1.490	3.451	1.451	2.000	-0.2	3	planar
BP	3.213	1.075	1.074	3.719	1.855	1.864	-5.7	8	planar
BAs	3.391	0.965	1.069	3.750	1.958	1.792	-5.2	12	planar
BSb	3.738	3.707	1.005	2.527	2.158	0.369	180.3	195	buckled
AlN	3.126	7.194	1.888	2.763	1.805	0.958	-644.6	65	planar
GaN	3.254	5.765	1.680	3.038	1.879	1.159	-295.1	31	planar
InN	3.638	13.837	1.708	2.673	2.100	0.573	-464.3	103	buckled
SiC	3.096	2.895	1.342	3.566	1.787	1.779	-132.0	12	planar
GeC	3.263	2.780	1.269	3.667	1.884	1.783	1.7	11	planar
SnC	3.604	4.415	1.301	3.531	2.081	1.450	-187.9	17	planar

of the out-of-plane electric polarization in bilayer BN [39], it would be reasonable to expect that the electric polarization reversal process can be also achieved in bilayer BP and BAs. In addition, the differential charge density of BP [see Fig. 2(d)] reveals that the out-of-plane electric polarization comes from the asymmetric charge redistributions as a result of the interlayer interaction, which is consistent with BN [39]. Due to the presence of the out-of-plane electric polarization, there exists a built-in electric field between the layers in the AC stacking configuration, which leads to a relative shift in the energy bands of the two layers. As shown in Fig. 2(g), the layer-projected band structure of BP in the AC stacking configuration reveals a type-II band alignment, where the valence band maximum and conduction band minimum derived from the lower and upper layer, respectively. Such alignments result in a reduction in global band gap. The type-II band alignment in these systems has also been reported in a previous work and demonstrates its appealing application in optoelectronic devices [54].

AlN, GaN, and InN have the same anion as BN. The calculated magnitudes of polarizations of AlN, GaN, and InN are 7.194, 5.765, and 13.837 pC/m, respectively. Compared with BN, the replacement of cation (B replaced by Al or Ga) increases the polarization by more than five times. The large electric polarization in AlN and GaN originates from the relatively stronger interlayer interactions, resulting in a more asymmetric charge redistribution, as clearly shown in Fig. 2(e), and the unusual large polarization in InN has the same origin as in BSb. The stronger interlayer interaction also significantly increases the energy barrier of the electric polarization reversal (see Table I), which may be disadvantageous to the high-speed data writing with low energy cost in devices [25]. Among them, the lowest translational sliding barrier between the AC and AB stacking configurations is 31 meV per unit cell for GaN, as shown in Fig. 2(b). Compared with BP, the energy bands of the lower and upper layer in bilayer GaN [see Fig. 2(h)] relatively shift by a larger amount, which gives rise to a large polarization, as shown in Table I.

The calculated magnitudes of electric polarizations in the AC stacking configuration of bilayer SiC, GeC, and SnC are 2.895, 2.780, and 4.415 pC/m, respectively, and the corre-

sponding energy barriers to reverse the electric polarization are 12, 11, and 17 meV per unit cell. As shown in Table I, their polarizations are significantly larger than that of BN and the energy barriers of the polarization reversal between the AC and AB stacking configurations are relatively low, which is favorable for devices based on sliding ferroelectricity. In particular, as shown in Fig. 2(c), both its polarization and the energy barrier for the reversal of electric polarization for GeC are somewhere between those of BP and GaN, which is consistent with the moderate charge redistribution between the layers [see Fig. 2(f)] and the medium relative shift between the energy bands of the lower and upper layers [see Fig. 2(i)].

C. Key factors underlying the magnitude of electric polarization

In the AC stacking configuration, all anions in the upper layer lie atop all cations in the lower layer, and all cations in the upper layer are right over the hexagon center of the lower layer. This stacking configuration breaks the inversion and mirror symmetries, which allows nonzero out-of-plane electric polarization that can be qualitatively understood by the distortion of the p_z orbital of the anions in the upper layer due to the Coulomb interactions between the layers. Therefore, the interlayer distance should be one of the main factors affecting the polarization. In order to reveal the dependence of the polarization on the interlayer distance, we first analyze the electric field generated by the lower layer in the AC stacking configuration based on the point-charge model. Then, the magnitude of the electric dipole moment per unit cell (p) can be roughly estimated by calculating the induced dipole moment of the anions in the upper layer under the electric field (see details in Note 1 in the Supplemental Material [53]), which is given as

$$p \propto \frac{C_0}{d^2 - R_0^2} - \frac{C_N}{\sqrt{L_N^2 + (d - R_N)^2}} + \frac{C_B}{\sqrt{L_B^2 + (d - R_B)^2}}, \quad (1)$$

where d is the interlayer distance and the others are material-related parameters. In the above relationship, the three terms on the right are derived from the cation from the lower layer

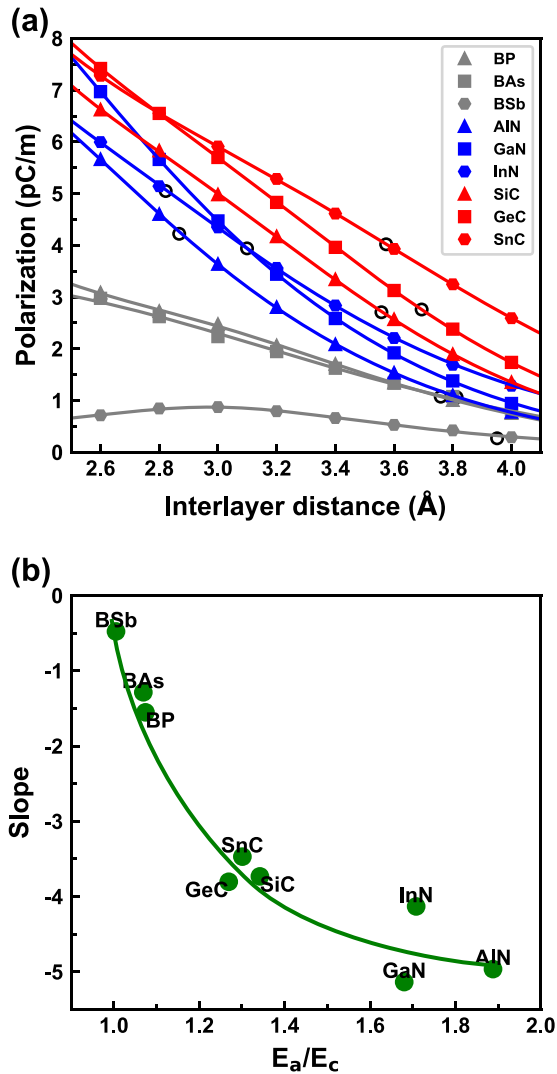


FIG. 3. Key factors underlying the magnitude of electric polarization. (a) Polarization as a function of the interlayer distance, where the black circles on the line refer to their equilibrium interlayer distances. (b) The slope of each material in (a) at its equilibrium interlayer distance versus the ratio of electronegativity of the two constituent elements, where the smooth solid line is used as a guide to the eye.

just below the anion from the upper layer, all the anions from the lower layer, and the other cations from the lower layer, respectively.

In order to check the validity of the relationship given in (1) for our studied system, we perform a series of constrained calculations in which all the atoms of each layer are allowed to be free only within in-plane directions and the distance between the layers are fixed to a series of preset values from 2.4 to 10.0 Å. The results show that the polarization generally decreases with the increase of the interlayer distance [see Figs. 3(a) and S7], which is intuitively expected. However, the polarization does not always increase as the interlayer distance decreases. For example, when the interlayer distance of BSb is less than 3 Å, the polarization decreases as the interlayer distance decreases, which may be due to that the van

der Waals (vdW) interaction is no longer dominant. Overall, the data can be well fitted by the above formula (see solid lines in Fig. S7 and the corresponding fitting parameters in Table S1 in the Supplemental Material [53]), which demonstrates the credibility of the aforementioned physical picture that uncovers the primary origin for sliding ferroelectricity in our studied systems. It is also worth noting that the relationship holds only at near the equilibrium interlayer distance and beyond, since the van der Waals interaction is no longer dominant at too small interlayer distance and the simple point-charge model fails.

Besides the dependence on interlayer distances, the magnitude of electric polarization also shows plain differences in the trends for different constituent materials. To understand this distinction qualitatively, we introduce the electronegativity, a basic chemical property that describes the tendency of an atom to attract electrons towards itself. In different constituent materials, the ratio of electronegativity of the two constituent elements is related to the bonding of ions and thus affects the magnitude of polarization. Here, the ratio of electronegativity of the two constituent elements is calculated by E_a/E_c , where E_a and E_c are the electronegativity of the anions and cations, respectively. The electronegativity values of elements use the Pauling scale [55], which is the most commonly used. The results are summarized in Table I. Specifically, as shown in Fig. 3(a), the electric polarization of BX ($X = P, As, Sb$) increases slowly with decreasing the interlayer distance, due to its particularly small ratio of electronegativity (~ 1.05). In contrast, the polarization of YN ($Y = Al, Ga, In$), which has a large ratio of electronegativity (~ 1.76), increases rapidly with decreasing the interlayer distance. For ZC ($Z = Si, Ge, Sn$) with a medium ratio of electronegativity (~ 1.30), its polarization increases approximately linearly with decreasing the interlayer distance. Furthermore, we calculate the slope of each material in Fig. 3(a) at its equilibrium interlayer distance, and plot it with the ratio of electronegativity of the two constituent elements [see Fig. 3(b)]. Overall, the larger the ratio of electronegativity, the larger the absolute value of the slope, which means that the magnitude of electric polarization near the equilibrium interlayer distance changes faster when the interlayer distance changes. However, for the same interlayer distance, it is not that the greater the ratio of electronegativity, the greater the magnitude of polarization [see Fig. 4(a)].

So far, we have discussed the relationship between the out-of-plane electric polarization and the interlayer distance, and the dependence of the change of the electric polarization with the interlayer distance on the electronegativity of the constituent elements for each material. Now it is meaningful to examine the polarizations of all the studied materials at their optimal interlayer distances for a unified picture. The dependence of the polarization on the electronegativity ratio and the optimal interlayer distance is shown in Figs. 4(b) and 4(c). Although there is a trend that the larger the optimal interlayer distance, the smaller the electric polarization, and the bigger the ratio of electronegativity, the greater the electric polarization, many data points deviate significantly. The reason may be that the optimal interlayer distance and the ratio of electronegativity are not independent of each other. Figure 4(d) shows the dependence of the optimal interlayer distance and the ratio of electronegativity, clearly indicating

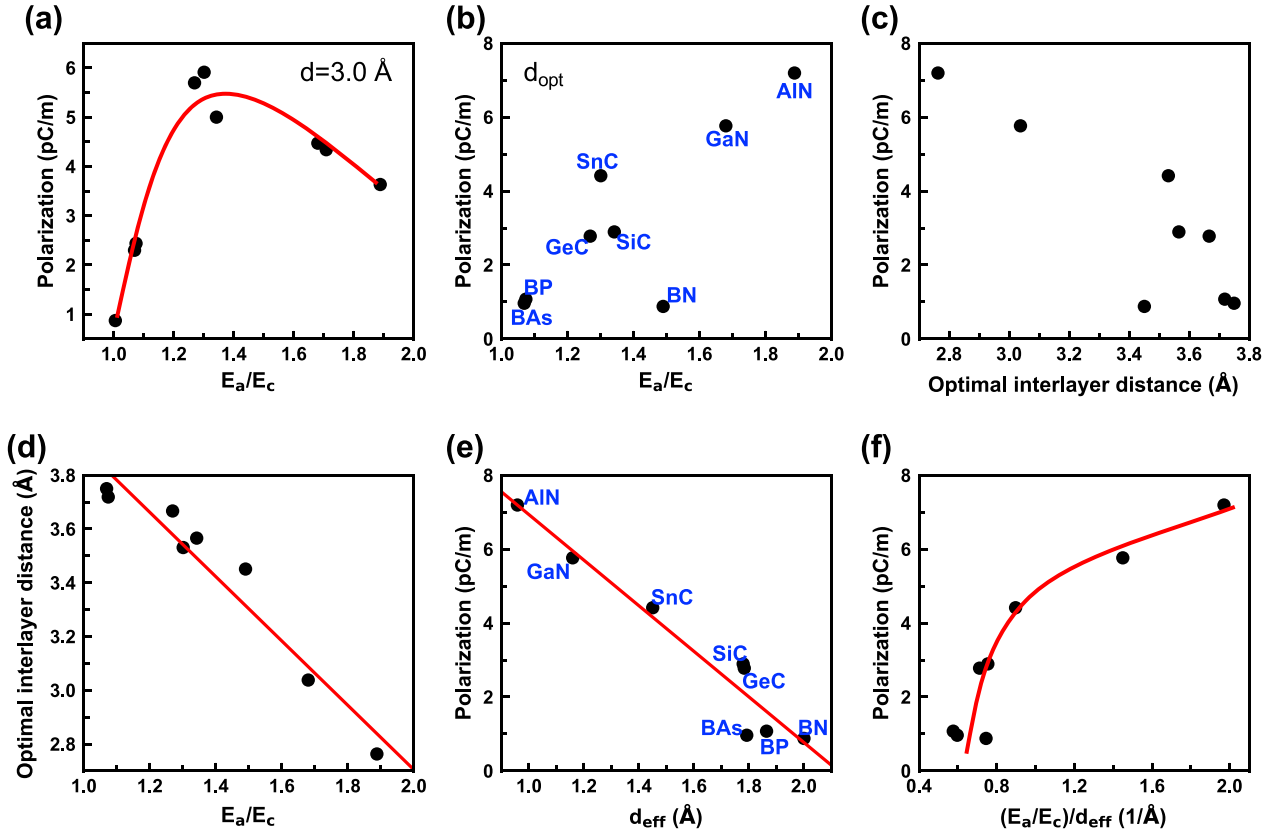


FIG. 4. Polarization versus the ratio of electronegativity at the same interlayer distance (a) and the respective optimal interlayer distance (b). (c) Polarization versus the respective optimal interlayer distance. (d) Optimal interlayer distance versus the ratio of electronegativity. (e) Polarization versus the effective distance. (f) Polarization versus the ratio of electronegativity of the two constituent elements divided by the effective distance.

the quasilinear correlation. The dependence complicates the relationship between the polarization and the optimal interlayer distance (the ratio of electronegativity) for different systems. Here, an effective distance is adopted and defined as $d_{\text{eff}} = d_{\text{opt}} - d_{\text{bond}}$, where d_{opt} and d_{bond} are the optimal interlayer distance and the length of covalent bond between the two elements within the monolayer, respectively. The correlation between the effective distance and the corresponding polarization of different systems is quasilinear [Fig. 4(e)], and this correlation is significantly stronger than that between the interlayer distance and the polarization [Fig. 4(c)]. Thus, we conclude that the effective distance is more appropriate than the optimal interlayer distance to describe the relationship between polarization and interlayer distance. From Table I and Fig. 4(e), it is clear that, compared with BN, the effective distance of all considered systems decreases, resulting in the increase of the polarization. Specifically, a slight decrease in the effective distance of BP and BAs (by ~ 0.17 Å) favors the increase of the electric polarization, whereas a significant reduction in the ratio of electronegativity (by ~ 0.42) counteracts its increase, ultimately resulting in only a slight increase in the electric polarization. For AlN and GaN, the significant decrease of the effective distance (by ~ 0.94 Å) and the increase of the ratio of electronegativity (by ~ 0.29) are both favorable for the increase of the electric polarization, and thus their magnitudes increase significantly. The effective distances (the ratio of electronegativity) of SiC, GeC,

and SnC are reduced by 0.22, 0.22, and 0.55 Å (0.15, 0.22, and 0.19), respectively, compared with that of BN, which is favorable (slightly unfavorable) for the increase of the polarization. The magnitude of electric polarization of SnC is about twice that of SiC or GeC, which is mainly attributed to the largely reduced effective distance. These results indicate that the magnitude of the polarization is affected by the combination of the effective distance (d_{eff}) and the ratio of electronegativity (E_a/E_c). To clearly demonstrate their correlation, we plot the polarization magnitude as a function of $(E_a/E_c)/d_{\text{eff}}$ in Fig. 4(f). It can be seen that, for our studied sliding ferroelectrics, the smaller the effective distance and the larger the difference in electronegativity of the two constituent elements, the larger the magnitude of electric polarization. This qualitative physical picture seems to work for other sliding ferroelectric systems. For example, the magnitudes of polarizations in bilayer MX_2 ($M = \text{Mo}$ and W , $X = \text{S}$ and Se) are smaller than that in bilayer BN [41], which can be understood by the larger effective distance (approximately the van der Waals interlayer distance d) and the smaller ratio of electronegativity (~ 1.15).

D. Stability of the polar stacking configurations

Now we turn our focus to the relative stability of the six high-symmetric stacking configurations given in Fig. 1(a). Starting with the AA and AA' stacking, a thorough search

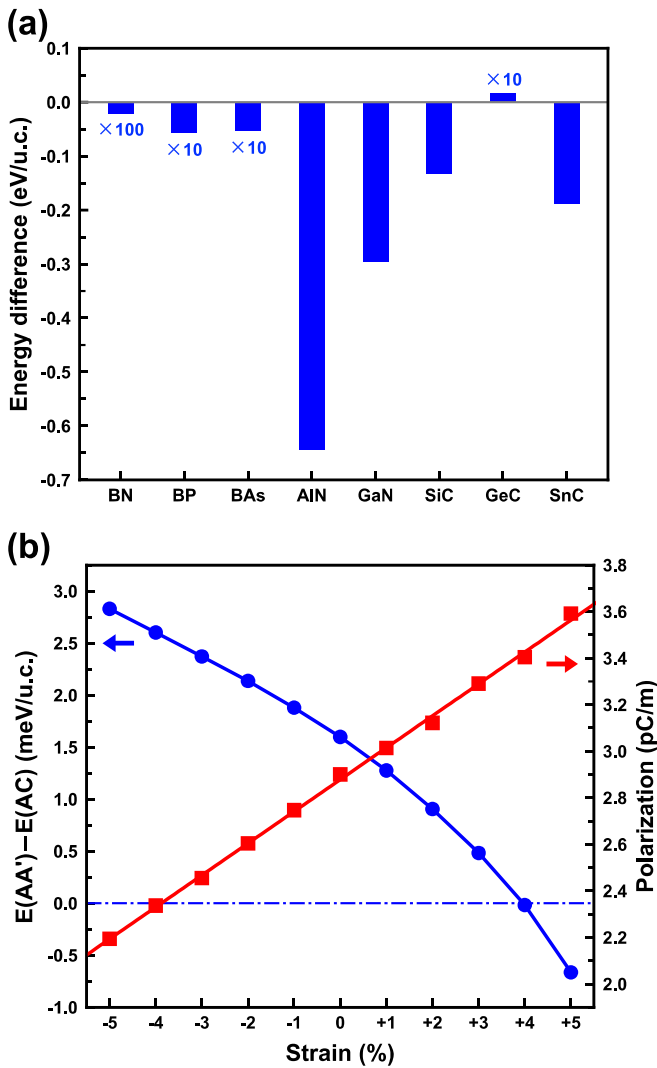


FIG. 5. (a) Energy differences of the AA' (AC' for BP and BAs) stacking configuration with respect to the AC. (b) Strain dependence of the energy difference (blue line) and the magnitude of polarization (red line) on the strain for AC stacking configuration of GeC, where the blue dash-dot line indicates the position where the energy difference is zero.

for possible stacking configurations along the high-symmetric paths is conducted and the results of several representative systems are shown in Fig. S1 in the Supplemental Material [53], which indicates that the extreme points in potential energy correspond to the six high-symmetric stacking configurations. For an instance, the most stable stacking configuration of bilayer BN is AA', a centrosymmetric van der Waals structure prohibiting electric polarization, of which the calculated total energy is 0.2 meV per unit cell lower than that of AC stacking, which is consistent with the previous results [56,57]. Similarly, the relative stability of the six high-symmetry stacking configurations in bilayer BX ($X = P, As, Sb$), YN ($Y = Al, Ga, In$), and ZC ($Z = Si, Ge, Sn$) is investigated. As shown in Fig. S8 in the Supplemental Material [53], the two energetically degenerate polar stacking configurations (AC and AB) are locally stable. Figure 5(a) gives the calculated energy differences (by the blue bars) of

the centrosymmetric stacking configuration AA' (AC' for BP and BAs) with respect to the polar stacking AC. For most systems, the centrosymmetric stacking configuration (AA' or AC') is the most energetically stable, except for GeC of which the polar stacking AC is globally stable. The stability of the polar stacking AC of GeC is further confirmed by the results of different vdW functions (Fig. S9) as well as the phonon spectra (Fig. S10), as detailed in the Supplemental Material [53]. Such behavior for GeC, consistent with the previous work [58,59], suggests that the sliding ferroelectricity may be easily achieved experimentally in GeC.

We further investigate the stability of the polar stacking configuration AC of GeC under strain. Figure 5(b) shows the calculated energy difference of the AA' stacking configuration with respect to the AC in various strains, where the positive value (blue line) indicates that the AC stacking is more energetically stable. The energy difference increases (decreases) with the increase of in-plane compressive (tensile) strain, indicating that the compressive (tensile) lattice is favorable (unfavorable) to stabilize the polar stacking configuration. When the tensile strain is larger than $\sim 4\%$, the energy difference becomes negative, indicating that the AA' stacking configuration with inversion symmetry is more stable. Meanwhile, the dependence of the polarization of AC stacking configuration on the strain is shown by the red line in Fig. 5(b), where the tensile (compressive) strain slightly increases (decreases) the electric polarization.

IV. CONCLUSION

In summary, we have examined the electric polarization, the energy barriers of the polarization reversal, and the electronic structure in bilayer BX ($X = P, As, Sb$), YN ($Y = Al, Ga, In$), and ZC ($Z = Si, Ge, Sn$), respectively, based on DFT calculations. It is shown that the magnitude of electric polarization decreases (increases) with the increase of the interlayer distance (the difference in electronegativity of the two constituent elements). Such qualitative relationship is further corroborated by a simple model based on the assumption that the out-of-plane electric polarization in the sliding ferroelectricity of the considered materials can be understood by the distortion of the p_z orbital of the anions sitting atop cations due to the Coulomb interactions between the layers. Therefore, to search for 2D sliding ferroelectrics with large out-of-plane polarization, the effective interlayer distance and the difference in electronegativity of the two constituent elements should be taken into consideration. In addition, our calculations for the stability of various stacking configurations reveal that GeC can be an ideal sliding ferroelectric candidate due to its large polarization and most stable polar stacking configuration. Our results thus can facilitate the search and design of functional 2D sliding ferroelectrics with large out-of-plane polarization.

ACKNOWLEDGMENTS

This work was financially supported by the Ministry of Science and Technology of the People's Republic of China (Grant No. 2022YFA1402903), the National Natural Science Foundation of China under Grant No. 12004160, and

the Open Project of Guangdong Provincial Key Laboratory of Magnetoelectric Physics and Devices under Grant No. 2020B1212060030. Z.G. also acknowledges the financial support from Shenzhen Science and Technology Program (Grant No. KQTD20190929173815000), Guangdong Innovative and Entrepreneurial Research Team Program (Grant No. 2019ZT08C044), and the Guangdong Provincial Key Labo-

ratory of Computational Science and Material Design (Grant No. 2019B030301001). The computer time was supported by the Center for Computational Science and Engineering of SUSTech and the Major Science and Technology Infrastructure Project of Material Genome Big-science Facilities Platform supported by Municipal Development and Reform Commission of Shenzhen.

- [1] W. Han, R. K. Kawakami, M. Gmitra, and J. Fabian, *Nat. Nanotechnol.* **9**, 794 (2014).
- [2] J. F. Sierra, J. Fabian, R. K. Kawakami, S. Roche, and S. O. Valenzuela, *Nat. Nanotechnol.* **16**, 856 (2021).
- [3] J. R. Schaibley, H. Yu, G. Clark, P. Rivera, J. S. Ross, K. L. Seyler, W. Yao, and X. Xu, *Nat. Rev. Mater.* **1**, 16055 (2016).
- [4] Q. H. Wang, K. Kalantar-Zadeh, A. Kis, J. N. Coleman, and M. S. Strano, *Nat. Nanotechnol.* **7**, 699 (2012).
- [5] G. Fiori, F. Bonaccorso, G. Iannaccone, T. Palacios, D. Neumaier, A. Seabaugh, S. K. Banerjee, and L. Colombo, *Nat. Nanotechnol.* **9**, 768 (2014).
- [6] F. H. L. Koppens, T. Mueller, Ph. Avouris, A. C. Ferrari, M. S. Vitiello, and M. Polini, *Nat. Nanotechnol.* **9**, 780 (2014).
- [7] M. Wu and P. Jena, *WIREs Comput. Mol. Sci.* **8**, e1365 (2018).
- [8] Z. Guan, H. Hu, X. Shen, P. Xiang, N. Zhong, J. Chu, and C. Duan, *Adv. Electron. Mater.* **6**, 1900818 (2020).
- [9] L. Qi, S. Ruan, and Y. Zeng, *Adv. Mater.* **33**, 2005098 (2021).
- [10] F. Xue, J.-H. He, and X. Zhang, *Appl. Phys. Rev.* **8**, 021316 (2021).
- [11] S. M. Neumayer, E. A. Eliseev, M. A. Susner, A. Tselev, B. J. Rodriguez, J. A. Brehm, S. T. Pantelides, G. Panchapakesan, S. Jesse, S. V. Kalinin, M. A. McGuire, A. N. Morozovska, P. Maksymovych, and N. Balke, *Phys. Rev. Mater.* **3**, 024401 (2019).
- [12] J. Wu, H.-Y. Chen, N. Yang, J. Cao, X. Yan, F. Liu, Q. Sun, X. Ling, J. Guo, and H. Wang, *Nat. Electron.* **3**, 466 (2020).
- [13] X. Wang, P. Yu, Z. Lei, C. Zhu, X. Cao, F. Liu, L. You, Q. Zeng, Y. Deng, C. Zhu, J. Zhou, Q. Fu, J. Wang, Y. Huang, and Z. Liu, *Nat. Commun.* **10**, 3037 (2019).
- [14] A. Belianinov, Q. He, A. Dziazgys, P. Maksymovych, E. Eliseev, A. Borisevich, A. Morozovska, J. Banys, Y. Vysochanskii, and S. V. Kalinin, *Nano Lett.* **15**, 3808 (2015).
- [15] F. Liu, L. You, K. L. Seyler, X. Li, P. Yu, J. Lin, X. Wang, J. Zhou, H. Wang, H. He, S. T. Pantelides, W. Zhou, P. Sharma, X. Xu, P. M. Ajayan, J. Wang, and Z. Liu, *Nat. Commun.* **7**, 12357 (2016).
- [16] S. Zhou, L. You, H. Zhou, Y. Pu, Z. Gui, and J. Wang, *Front. Phys.* **16**, 13301 (2021).
- [17] J. Xiao, H. Zhu, Y. Wang, W. Feng, Y. Hu, A. Dasgupta, Y. Han, Y. Wang, D. A. Muller, L. W. Martin, P. A. Hu, and X. Zhang, *Phys. Rev. Lett.* **120**, 227601 (2018).
- [18] F. Xue, W. Hu, K. Lee, L. Lu, J. Zhang, H. Tang, A. Han, W. Hsu, S. Tu, W. Chang, C. Lien, J. He, Z. Zhang, L. Li, and X. Zhang, *Adv. Funct. Mater.* **28**, 1803738 (2018).
- [19] S. Mukherjee and E. Koren, *Isr. J. Chem.* **62**, e202100112 (2022).
- [20] S. Yuan, X. Luo, H. L. Chan, C. Xiao, Y. Dai, M. Xie, and J. Hao, *Nat. Commun.* **10**, 1775 (2019).
- [21] C. H. Ahn, K. M. Rabe, and J.-M. Triscone, *Science* **303**, 488 (2004).
- [22] W. Ding, J. Zhu, Z. Wang, Y. Gao, D. Xiao, Y. Gu, Z. Zhang, and W. Zhu, *Nat. Commun.* **8**, 14956 (2017).
- [23] L. Li and M. Wu, *ACS Nano* **11**, 6382 (2017).
- [24] E. Y. Tsymbal, *Science* **372**, 1389 (2021).
- [25] M. Wu and J. Li, *Proc. Natl. Acad. Sci. U.S.A.* **118**, e2115703118 (2021).
- [26] Y. Liang, S. Shen, B. Huang, Y. Dai, and Y. Ma, *Mater. Horiz.* **8**, 1683 (2021).
- [27] W. Jiang, C. Liu, X. Ma, X. Yu, S. Hu, X. Li, L. A. Burton, Y. Liu, Y. Chen, P. Guo, X. Kong, L. Bellaiche, and W. Ren, *Phys. Rev. B* **106**, 054104 (2022).
- [28] Q. Yang, M. Wu, and J. Li, *J. Phys. Chem. Lett.* **9**, 7160 (2018).
- [29] X. Liu, Y. Yang, T. Hu, G. Zhao, C. Chen, and W. Ren, *Nanoscale* **11**, 18575 (2019).
- [30] Z. Lin, C. Si, S. Duan, C. Wang, and W. Duan, *Phys. Rev. B* **100**, 155408 (2019).
- [31] X. Liu, A. P. Pyatakov, and W. Ren, *Phys. Rev. Lett.* **125**, 247601 (2020).
- [32] T. Zhang, Y. Liang, X. Xu, B. Huang, Y. Dai, and Y. Ma, *Phys. Rev. B* **103**, 165420 (2021).
- [33] N. Ding, J. Chen, C. Gui, H. You, X. Yao, and S. Dong, *Phys. Rev. Mater.* **5**, 084405 (2021).
- [34] X. Ma, C. Liu, W. Ren, and S. A. Nikolaev, *npj Comput. Mater.* **7**, 177 (2021).
- [35] T. Zhang, X. Xu, B. Huang, Y. Dai, and Y. Ma, *npj Comput. Mater.* **8**, 64 (2022).
- [36] T. Zhong, Y. Ren, Z. Zhang, J. Gao, and M. Wu, *J. Mater. Chem. A* **9**, 19659 (2021).
- [37] Y. Liang, N. Mao, Y. Dai, L. Kou, B. Huang, and Y. Ma, *npj Comput. Mater.* **7**, 172 (2021).
- [38] Y. Liang, R. Guo, S. Shen, B. Huang, Y. Dai, and Y. Ma, *Appl. Phys. Lett.* **118**, 012905 (2021).
- [39] K. Yasuda, X. Wang, K. Watanabe, T. Taniguchi, and P. Jarillo-Herrero, *Science* **372**, 1458 (2021).
- [40] M. Vizner Stern, Y. Waschitz, W. Cao, I. Nevo, K. Watanabe, T. Taniguchi, E. Sela, M. Urbakh, O. Hod, and M. Ben Shalom, *Science* **372**, 1462 (2021).
- [41] X. Wang, K. Yasuda, Y. Zhang, S. Liu, K. Watanabe, T. Taniguchi, J. Hone, L. Fu, and P. Jarillo-Herrero, *Nat. Nanotechnol.* **17**, 367 (2022).
- [42] Z. Fei, W. Zhao, T. A. Palomaki, B. Sun, M. K. Miller, Z. Zhao, J. Yan, X. Xu, and D. H. Cobden, *Nature (London)* **560**, 336 (2018).
- [43] Y. Wan, T. Hu, X. Mao, J. Fu, K. Yuan, Y. Song, X. Gan, X. Xu, M. Xue, X. Cheng, C. Huang, J. Yang, L. Dai, H. Zeng, and E. Kan, *Phys. Rev. Lett.* **128**, 067601 (2022).

- [44] G. Kresse and J. Furthmüller, *Phys. Rev. B* **54**, 11169 (1996).
- [45] P. E. Blöchl, *Phys. Rev. B* **50**, 17953 (1994).
- [46] G. Kresse and D. Joubert, *Phys. Rev. B* **59**, 1758 (1999).
- [47] J. P. Perdew, K. Burke, and M. Ernzerhof, *Phys. Rev. Lett.* **77**, 3865 (1996).
- [48] M. Methfessel and A. T. Paxton, *Phys. Rev. B* **40**, 3616 (1989).
- [49] G. Henkelman, B. P. Uberuaga, and H. Jónsson, *J. Chem. Phys.* **113**, 9901 (2000).
- [50] S. Grimme, J. Antony, S. Ehrlich, and H. Krieg, *J. Chem. Phys.* **132**, 154104 (2010).
- [51] A. Togo and I. Tanaka, *Scr. Mater.* **108**, 1 (2015).
- [52] H. Şahin, S. Cahangirov, M. Topsakal, E. Bekaroglu, E. Akturk, R. T. Senger, and S. Ciraci, *Phys. Rev. B* **80**, 155453 (2009).
- [53] See Supplemental Material at <http://link.aps.org/supplemental/10.1103/PhysRevB.107.035426> for more details on the bilayer structures with lateral shift and their corresponding polarizations, relative energies, and interlayer distances, and the model analysis on the effect of interlayer distance on the magnitude of the out-of-plane electric polarization.
- [54] Q. Wang, Y. Liang, H. Yao, J. Li, T. Liu, T. Frauenheim, B. Wang, and J. Wang, *J. Mater. Chem. C* **10**, 1048 (2022).
- [55] A. L. Allred and J. Inorg, *Nucl. Chem.* **17**, 215 (1961).
- [56] G. Constantinescu, A. Kuc, and T. Heine, *Phys. Rev. Lett.* **111**, 036104 (2013).
- [57] S. M. Gilbert, T. Pham, M. Dogan, S. Oh, B. Shevitski, G. Schumm, S. Liu, P. Ercius, S. Aloni, M. L. Cohen, and A. Zettl, *2D Mater.* **6**, 021006 (2019).
- [58] Z. Xu, Y. Li, C. Li, and Z. Liu, *Appl. Surf. Sci.* **367**, 19 (2016).
- [59] S. A. Tawfik, T. Gould, C. Stampfl, and M. J. Ford, *Phys. Rev. Mater.* **2**, 034005 (2018).